

Internal and external modulation of folding rates with 104 to 105 year time resolutions from growth strata, Pico del Aguila, Spain

Dave Anastasio¹, Kenneth Philip Kodama¹, Josep Parés², Linda Hinnov³, and Bruce D. Idleman¹

¹Lehigh University

²Geochronology Group, CENIEH, Paseo Sierra de Atapuerca 3, 09002 Burgos, Spain

³George Mason University

November 26, 2022

Abstract

High-resolution cyclostratigraphy in growth strata are used to reconstruct unsteady folding rates at the regional-scale Pico del Aguila anticline, southern Pyrenees, to evaluate deformation modulation. Magnetic polarity stratigraphy was used to determine absolute time and to calibrate cyclostratigraphy-based anhysteretic remanent magnetization intensity variations to establish precessional frequencies in the growth strata record. Incremental tilting rates were calculated between selected horizons over ~ 5.24 myr of fold growth. Careful treatment of uncertainties enhances confidence that the results are meaningful and results show significant variability in folding rates over time. The acceleration phase of fold growth was variable, punctuated by a prolonged period of tectonic quiescence, and correlated to sedimentation changes in the wedge-top basin. Shallow-dipping bedding intrinsically modulated the initial rates of folding for the first 25% of limb tilt until 38.9 Ma. Then, halotectonics in the Paleogene Jaca Basin extrinsically modulated accelerating folding rates for the next 42% of folding, until ~ 37.5 Ma. Finally, forelimb-steepening leading to geometric strain hardening and blunted folding rates for the last 21% of fold tightening and causing a thrust fault to cut the anticline's core. Folding ended at Pico del Aguila ~ 35.9 Ma. Calculated folding rates varied between $0^\circ \pm 5.5^\circ$ and $90^\circ \pm 19^\circ$ /myr over 100s kyr time increments. Variations in the folding rate of the Pico del Aguila décollement anticline are attributed to both intrinsic modulation as a result of progressive bedding steepening during folding and extrinsic modulation as a result of variable deltaic sedimentation rates in the wedge-top basin.

1 **Internal and external modulation of folding rates with 10^4 to 10^5 year time resolutions from**
2 **growth strata, Pico del Aguila, Spain**

3 **David J. Anastasio¹, Kenneth P. Kodama¹, Josep M. Parés², Linda A. Hinnov³, Bruce D.**
4 **Idleman¹**

5 ¹Lehigh University, Earth & Environmental Sciences, 1 W. Packer Ave., Bethlehem, PA, 18015-
6 3001 USA

7 ²Centro Nacional de Investigación sobre la Evolución Humana, Department of Geochronology
8 and Geology, Paseo Sierra de Atapuerca 3, Burgos, 090002, Spain

9 ³George Mason University, Department of Atmospheric, Oceanic, and Earth Science, Fairfax,
10 VA, 22030 USA

11

12 Corresponding author: David Anastasio (dja2@lehigh.edu)

13

14 **Key points:**

15 • variable folding rates, between 5.5° and $90^\circ \pm 19^\circ$ /myr over 100s kyr time increments,
16 characterize Pico del Aguila anticline, Spain

17 • deformation rates are modulated by both intrinsic processes and extrinsic processes

18

19 **ABSTRACT**

20 High-resolution cyclostratigraphy in growth strata are used to reconstruct unsteady folding
21 rates at the regional-scale Pico del Aguila anticline, southern Pyrenees, to evaluate deformation
22 modulation. Magnetic polarity stratigraphy was used to determine absolute time and to
23 calibrate cyclostratigraphy-based anhysteretic remanent magnetization intensity variations to
24 establish precessional frequencies in the growth strata record. Incremental tilting rates were
25 calculated between selected horizons over ~5.24 myr of fold growth. Careful treatment of
26 uncertainties enhances confidence that the results are meaningful and results show significant
27 variability in folding rates over time. The acceleration phase of fold growth was variable,
28 punctuated by a prolonged period of tectonic quiescence, and correlated to sedimentation
29 changes in the wedge-top basin. Shallow-dipping bedding intrinsically modulated the initial
30 rates of folding for the first 25° of limb tilt until 38.9 Ma. Then, halotectonics in the Paleogene
31 Jaca Basin extrinsically modulated accelerating folding rates for the next 42° of folding, until
32 ~37.5 Ma. Finally, forelimb-steepening leading to geometric strain hardening and blunted
33 folding rates for the last 21° of fold tightening and causing a thrust fault to cut the anticline's
34 core. Folding ended at Pico del Aguila ~35.9 Ma. Calculated folding rates varied between 0°±
35 5.5° and 90° ± 19°/myr over 100s kyr time increments. Variations in the folding rate of the Pico
36 del Aguila décollement anticline are attributed to both intrinsic modulation as a result of
37 progressive bedding steepening during folding and extrinsic modulation as a result of variable
38 deltaic sedimentation rates in the wedge-top basin.

39 **Plain Language Summary**

40 A high-resolution age model, with careful consideration to uncertainties, is used to reconstruct
41 deformation rates at Pico del Aguila, Spain. The age model is recovered from sedimentary rocks
42 that were deposited during deformation using magnetic methods. Deformation exceeded 5.24
43 million years with variable speed. Variations in deformation rate are attributed to both internal
44 and external causes.

45 **1 INTRODUCTION**

46 Geometric interpretations and chronologic data suggest that deformation in orogens is
47 unsteady at all timescales, from rates determined from GPS geodesy (10^{-1} yr), seismology (10^0
48 to 10^1 yr), paleoseismology (10^2 to 10^3 yr), magnetostratigraphy (10^4 to 10^6 yr),
49 biostratigraphically (10^5 to 10^6 yr) or isotopically dated synsedimentary structures (10^5 to 10^6
50 yr) (e.g., Suppe et al., 1992; Gundersen et al., 2013). But what processes modulate this
51 deformation rate unsteadiness? In this paper, we focus on the 10^4 to 10^6 year timescales of
52 folding.

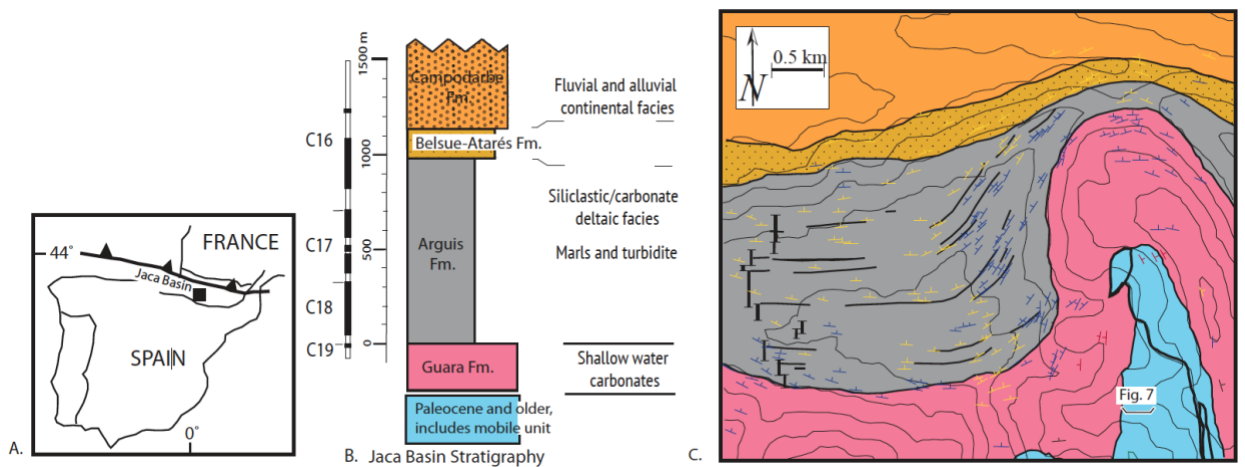
53 At these timescales, intrinsic drivers of the deformation rate might include such
54 processes as strain partitioning (e.g., Bennett et al., 2004), fault growth and linkage (e.g.,
55 McCartney and Scholz, 2016), stress fluctuations (e.g., Gold et al., 2017), or strain hardening
56 and softening resulting from changes in deformation mechanism or orientation of anisotropy
57 (e.g., Donath 1962; Donath and Parker, 1964; Ramsay, 1967; Dolan et al., 2016). Extrinsic
58 factors that might affect deformation rates, i.e., those things that affect the system boundary
59 conditions, include such things as variable plate forcing (e.g., Holl and Anastasio, 1995),
60 changes in surface loads affecting the stress state of faults (e.g., Hampel and Hetzel, 2005),
61 pore pressure transience (e.g., Shaffer and Tobin, 2011; Gold et al., 2017), or synorogenic

62 sedimentation or erosion (e.g., Burbank et al., 2003).

63 The velocity and steadiness of deformation rates can provide clues to what modulates
64 the tectonic processes. Since growth strata record the combined influence of deformation and
65 deposition, deformation rates and incremental deformation geometry can be extracted from
66 well-dated and geometrically well-characterized growth strata geometries. In this study, a high-
67 resolution age model was recovered from marine and continental growth strata dated with
68 magnetic polarity stratigraphy and rock magnetic-based cyclostratigraphy determined at the
69 precessional timescale, i.e., ~20,000 yr for ~5.24 myr (Kodama et al., 2010). Fold geometry was
70 determined by down-plunge projection of precision GPS locations, interpretation of fold growth
71 strata from 1:5000 orthophotographs, and 1:5000 scale DEM analysis of growth strata
72 geometry to get a rare glimpse into the variation in folding rates through time and to reveal
73 changes in the processes that modulate deformation.

74 Pico del Aguila is a regional-scale décollement anticline with a thrust faulted core that
75 developed in the hanging wall of the frontal (Guarga) thrust sheet, External Sierras, Pyrenees,
76 Spain (**Fig. 1**). Folding developed above a mobile gypsiferous shale unit within the hundreds
77 of meter thick Triassic Keuper facies that floors an ~1 km thick stiffer unit in pre-growth
78 stratigraphy that is dominated by carbonate rocks of Cretaceous to Middle Eocene age
79 (Puideàbregas, 1975). There are also carbonate units within the Keuper facies that are
80 referred to as the Mushelkalk facies and which manifest themselves as a broken formation
81 (Mey et al., 1968), which includes cellular dolomite (Anastasio, 1992). The westward
82 prograding growth strata consist of marine, deltaic, and continental facies up to 1.34 km
83 thick, which eventually buried the anticline. Bedding in the growth strata on the western limb

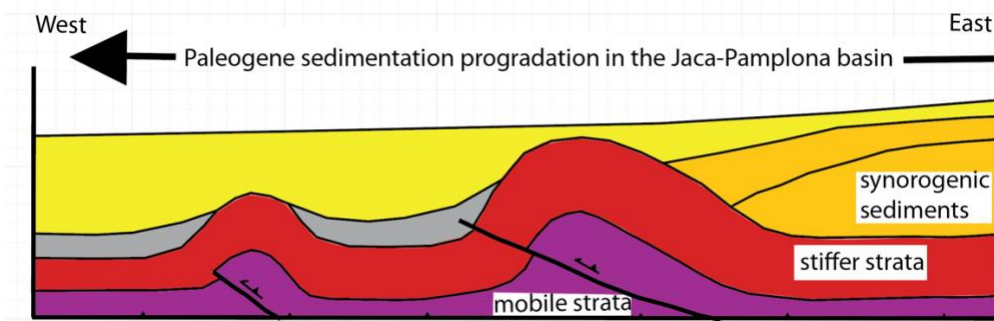
84 of the fold shallows from a near vertical dip in Late Eocene carbonates to horizontal bedding
 85 in the overlying Oligocene fluvial strata (**Fig. 1**). Most of the folding occurred during the Late
 86 Eocene Arguis Fm. deposition, a deltaic flysch unit characterized by mixed carbonate and
 87 siliciclastic sediment (Pudèfàbregas, 1975; Castelltort et al., 2003). A latest Lutitian to early
 88 Priabonian age of the Arguis Fm. is supported by multispecies biostratigraphy (Canudo, 1990;
 89 Canudo et al., 1991) and magnetic polarity stratigraphy (Hogan, 1993; Pueyo et al., 2002;
 90 Kodama et al., 2010; Rodríguez-Pinto et al., 2012; **Fig. 1**).



91 **Figure 1. A.** Index map showing Pico del Aguila (box) and the Jaca Basin in northern Spain. Pico
 92 del Aguila at solid square. **B.** Legend for stratigraphic units shown in **Figure 1C** and Jaca Basin
 93 magnetic polarity stratigraphy from Kodama et al. (2010), lithostratigraphy and environment of
 94 deposition. **C.** Geologic map of Pico del Aguila showing bedding measurements: shallow dip of
 95 bedding ($\leq 30^\circ$)-yellow, moderate dip ($31^\circ-60^\circ$)-blue and steep dip ($61^\circ-90^\circ$)-red. Stratigraphic
 96 section measured and samples for this study at the location of the bold black lines. UTM
 97 coordinates are shown at corners of the map.

98
 99
 100 The train of External Sierras folds developed by differential loading halotectonics
 101 processes along the southern margin of the south Pyrenees wedge-top Jaca Basin (Anastasio,

102 1992; **Fig. 2**). This process of mobile strata migration in response to a prograding overburden is
103 similar to the ongoing folding in the Gulf of Mexico (e.g. Bishop 1978; Ge et al., 1997). Pico del
104 Aguila deformation overlapped in time with Guarga thrust sheet emplacement and wedge-top
105 basin deposition (Anastasio, 1992).



106
107 **Figure 2.** Sketch of differential loading halotectonics, with transverse folding in the hanging wall
108 of the schematic Guarga thrust sheet resulting from progradation of Paleogene synorogenic
109 sediments in the Pyrenean wedge-top basin. Transverse folds develop in response to the
110 prograding overburden.

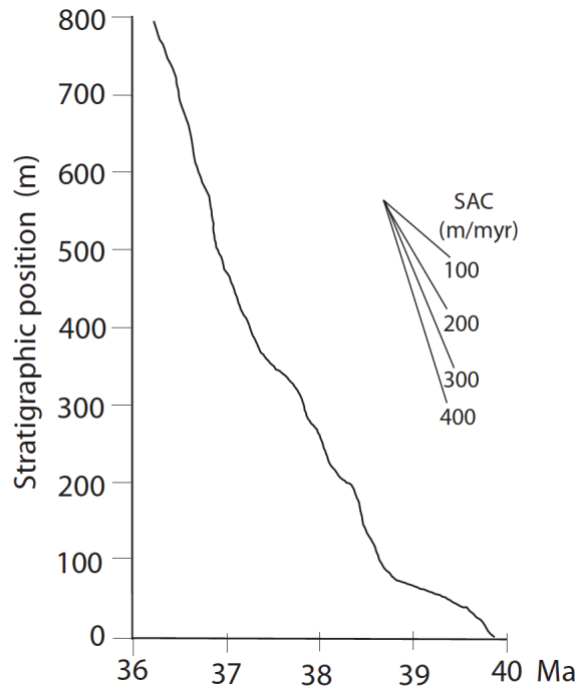
111
112 There have been many previous studies at Pico del Aguila anticline, including Puidefàbregas
113 (1975), who mapped the Jaca Basin and studied the sedimentology of the Arguis Fm.,
114 Casselltort et al. (2003), who studied the stratigraphy of the growth strata around the anticline,
115 Hogan and Burbank (1996), who reconstructed geohistory from the area's first magnetic
116 polarity stratigraphy studies, Kodama et al. (2010), who used magnetic polarity stratigraphy and
117 cyclostratigraphy to determine the detailed age of the growth strata horizons, Poblet and Hardy
118 (1995), who analyzed growth strata geometries, and analogue and numerical modeling of the
119 fold growth by Vidal-Royo et al. (2012; 2013). Pico del Aguila is a well-known synsedimentary

120 structure, where high sedimentation-to-uplift rates provides growth strata that records folding
121 in high fidelity.

122 **2 METHODS AND RESULTS**

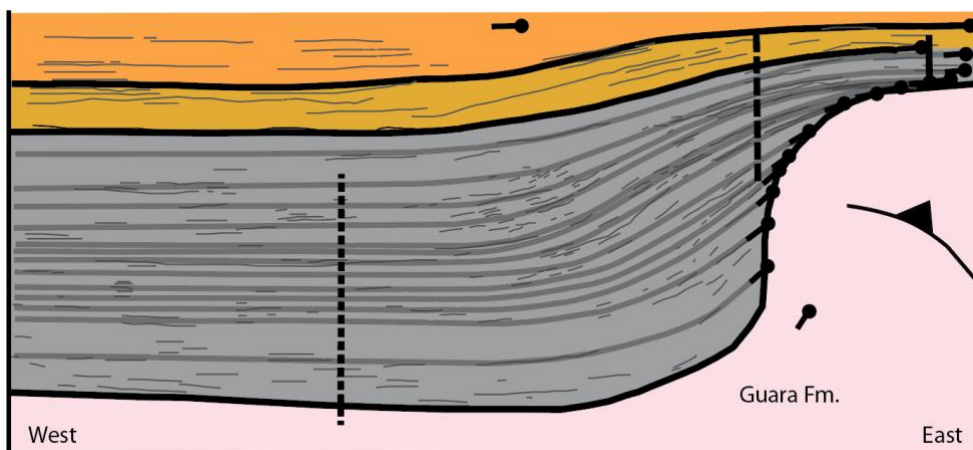
123 **2.1 Fold Geometry**

124 Pico del Aguila is a tight, asymmetric, westward overturned, moderately north plunging,
125 décollement anticline in the central External Sierras (e.g., Anastasio et al., 2015). The folding
126 developed in the shallow crust, at <3 km of depth (Hogan and Burbank 1996) and <60°C
127 (Anastasio and Holl, 2001). The fold geometry and fold orientation were determined during
128 field mapping as bedding data and formation contacts were collected (Anastasio, 1987). **Figure**
129 **3** shows that sedimentation accumulation rates increased during folding and that Pico del
130 Aguila was eventually buried by deltaic sediments (**Fig. 4**). The growth strata were mapped with
131 precision GPS using a local base station (cm scale accuracy), or with a handheld GPS with
132 barometric altimetry for elevation (m scale accuracy). To determine folding rates we also
133 interpreted growth strata on registered 1:5000 orthophotographs, on 1:5000 digital, 10m
134 elevation models, and took advantage of multiple measured sections (e.g. Puidefàbregas, 1975;
135 Castellort et al., 2003; this study) with uncertainty on bedding thickness determined by Jacob
136 staff or tape measure conservatively estimated at ± 5 m (1σ). Bedding locations, bedding
137 inclinations, and growth strata strike-lines were projected onto a dipping plane perpendicular
138 to the great circle defined by the average bedding orientations about the Pico del Aguila fold



139

140 **Figure 3.** Calibrated cyclostratigraphic age model of the stratigraphic column shown in **Figure**
 141 **1B.** The age model is based on La2004 precession index tuning of the ARM time series (Fig. 5.5
 142 in Kodama and Hinnov, 2014). Stratigraphic horizon ages were determined from the
 143 astrochronology, except first and last increments of folding where subchron averaged
 144 sedimentation rates were used to calculate the age model. SAC abbreviates sediment
 145 accumulation rate and line slopes show various SACs.



146

147 **Figure 4.** Down-plunge projection of Pico del Aguila anticline drawn perpendicular to the great
 148 circle (profile plane) defining the fold. The orientation of the projected plane strikes 090° and

149 *dips 67°S. Measured section locations at positions shown by vertical lines—shortest dash this*
150 *study, longer dashed line Castellort, 2003, and solid line from Puidefàbregas, 1975 and*
151 *Castellort, 2003. Stratigraphy colors as in **Figure 1**.*

152
153 (perpendicular to the fold axis). Mesoscopic faulting studies in pre-growth Guara limestones
154 (Anastasio and Holl, 2001) and studies of growth strata geometry and their penetrative fabric
155 (Anastasio et al., 2015) show that the Pico del Aguila anticline developed with fixed limb lengths
156 and limb shearing towards a pinned fold hinge. The rotation of the fold limbs is also recorded
157 by growth strata, which thin stratigraphically towards the anticlinal crest and shallow in dip, up-
158 section. Incremental folding rates were determined for the west dipping limb of the fold in 14
159 time increments using the cyclostratigraphy results from Kodama et al., (2010) and magnetic
160 stratigraphy results from Hogan and Burbank (1996), Kodama et al., (2010), and Rodriguez-Pintó
161 et al., (2012).

162 **2.2 Growth Strata Chronology**

163 Growth strata cyclostratigraphy was established in the Arguis syncline for a measured
164 and sampled section located and dated in detail (**Fig. 1**). From oldest to youngest, the growth
165 stratigraphy of the External Sierras consists of shallow water carbonates at the top of the Guara
166 Fm., marls and turbidites of the Arguis Fm., siliciclastic and carbonate deltaic facies of the
167 Belsue-Atarés Fm., and the fluvial continental facies of the Campodarbe Fm. (**Fig. 1B**). Most of
168 the folding at Pico del Aguila formed during the deposition of the Arguis Fm., the focus of our
169 chronologic investigations. There was a gradual increase in the sediment coarseness and
170 accumulation rates associated with delta progradation over top of the Pico del Aguila anticline
171 (**Figs. 3 and 4**; Kodama et al., 2010). The growth strata record uplift exceeding sediment

172 accumulation early during folding leading to the onlap of growth horizons and sediment
173 accumulation exceeding uplift at the end of folding leading to the growth strata burring the fold
174 (**Figs. 1 and 4**).

175 Magnetic polarity stratigraphy and rock magnetic-based cyclostratigraphy were used to
176 go from the stratigraphic depth domain to the time domain in the growth strata. A local
177 paleomagnetic stratigraphy was correlated to the Geomagnetic Polarity Time Scale (GPTS;
178 Gradstein et al., 2012) using existing biostratigraphy to establish absolute dates, assuming
179 polarity reversals were at the midpoint between sampling sites of opposite polarity. Magnetic
180 polarity reversals were then used to calibrate the anhysteretic remanent magnetization (ARM)
181 data series which was used as proxy for magnetite concentration variations in the measured
182 section. With a specimen analyzed every 3 kyr (nearly 1400 samples spaced 0.25-1.5m) and a
183 specimen size which only integrates sediment accumulation over a few centuries, the ARM data
184 series recovery of the cyclostratigraphy was robust. The detailed chronology of the growth
185 strata was presented in Kodama et al., (2010).

186 **2.3 Folding Rate Uncertainties**

187 On a scale of 10^4 to 10^6 yrs, folding was variable and unsteady through time (**Fig. 5**). This
188 conclusion includes a careful consideration of input uncertainties. In order to more easily
189 handle the various calculation methods needed to determine folding rates in different parts of
190 the section, the uncertainties were assessed using a Monte Carlo simulation. Uncertainties in
191 bedding measurement locations and bedding pole orientations were estimated to be $\pm 1^\circ$ by
192 down-plunge assessment or $\pm 1.5^\circ$ by repeated measurements with a geologic compass
193 (uncertainties quoted at the 1σ). Errors on the stratigraphic position of strike lines ranged from

194 $\pm 5 - 25$ m, depending on the depth in the growth section. Relative uncertainties in magnetic
195 chron ages were assumed to be ± 20 kyr, and uncertainties in chron positions within the section
196 were based on the paleomagnetic site spacing (3 m) that was determined by Jacob staff and
197 compass (**Fig. 5**). For the purposes of the Monte Carlo model, the stratigraphic positions of
198 paleomagnetic chron boundaries were allowed to vary with uniform weight over the full extent
199 of the sample spacing, whereas other uncertainties were assumed to be normally distributed.
200 Within the astronomically tuned portion of the section, depositional ages were determined by a
201 look up function for sediment accumulation rates determined by the cyclostratigraphy and
202 previously published in Kodama et al., (2010) (Fig. 9 in Kodama et al., 2010; **Fig 3**). Uncertainty
203 in relative time in this part of the section is estimated to be $\pm 10,000$ years (half a precessional
204 cycle), since the section was tuned at the precessional scale (Fig. 5.5 in Kodama and Hinnov,
205 2014). The model runs typically converged to better than 1% relative uncertainty in <100
206 iterations, but all of our quoted folding rate uncertainties are based on runs of 1000 iterations.

207 Site spatial errors and the correlation of the proxy ARM record to seasonal variations in
208 insolation are correlated and therefore were not propagated. Small but correlated errors due to
209 sample sizes (< few centuries) and orbital motions were also not propagated. All reported
210 astronomical ages include a ± 2.5 kyr error due to uncertainty in the season of insolation forcing.
211 Additional timing errors also played into the modeling uncertainties in some cases: the ages
212 used are likely 1 kyr too old due to application of the La1993 astronomical target (Laskar et al.,
213 1993) in Messinian tuning (e.g., Hilgen et al., 2007) compared with those of the La2004 target
214 (Laskar et al., 2004), and up to 2 kyr too old due to uncertainties in tidal dissipation (Lourens et
215 al., 2004). The beginning and end phases of folding were determined by bedding dip and

216 magnetic polarity stratigraphy, only (**Fig. 5**). During these increments the age errors were also
217 assigned to be $\pm 10,000$ yrs. Bedding inclination uncertainty was surprisingly the largest source
218 of error in the folding rate calculations. This uncertainty is attributed primarily to bedding
219 surface irregularities in the stratigraphic facies investigated, rather than to issues with the
220 measurement process itself.

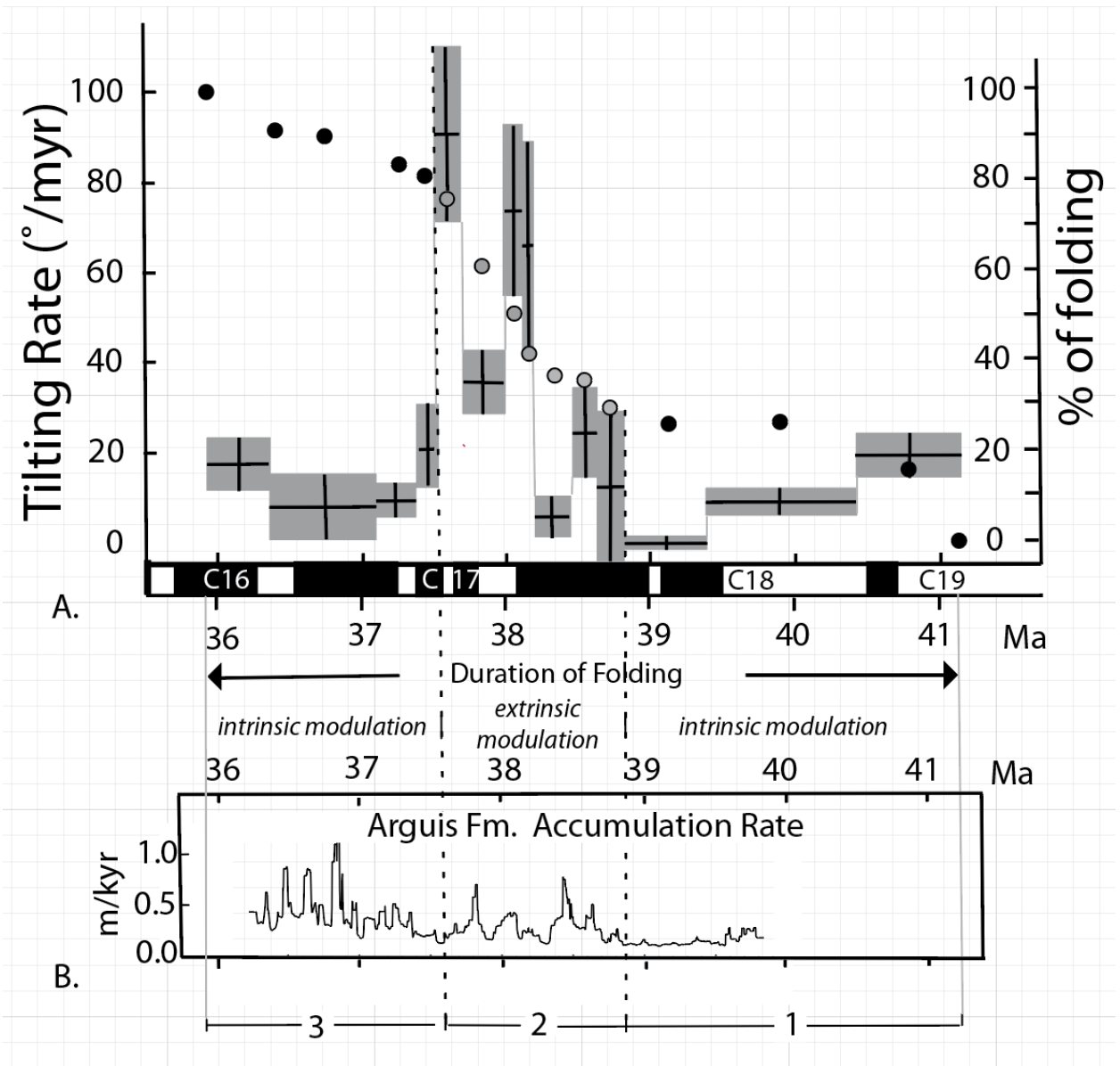
221 Overall, the limb tilt increased to a maximum and decreased abruptly as bedding
222 steepened and Pico del Aguila became buried (**Figs. 1 and 5**). Calculated folding rates varied
223 between $0^\circ \pm 5.5^\circ$ and $90^\circ \pm 19^\circ$ /myr over 100's kyr time increments and were in pace with
224 sedimentation rates. The fastest tilting rates occurred when bedding was at modest inclinations
225 and formation strength was lowest as predicted by flexural-slip folding kinematics with
226 mechanically-active bedding planes (**Fig 6**). Overall, sediment accumulation rates varied over
227 two orders of magnitude between $<0.1\text{m/kyr}$ and $>1\text{m/kyr}$ (**Fig. 5**).

228 **3 DISCUSSION**

229 Empirical results from this high-resolution study confirms some expectations of folding
230 but contradict others. Examination of **figure 5** shows that when chronologic resolution is only
231 by biostratigraphy or magnetic polarity stratigraphy, such as at the beginning and end of the
232 folding, the time resolution relative to cyclostratigraphy is degraded (e.g., Gunderson et al.,
233 2015). The uncertainty analysis shows that the folding rate in a deltaic sequence is most
234 sensitive to the bedding inclination change and time resolution between the assessments. As
235 predicted by buckling theory, a folding instability (e.g., Sherwin and Chapple, 1968) occurred as
236 a result of upstream delta progradation inducing E-W compression in the External Sierras
237 (Anastasio, 1992). Following the onset of folding, the folding rate increased more than five-fold

238 before slowing rapidly and finally ending ~5.24 myr after folding began.

239



240

241 **Figure 5.** Incremental fold rate assessment. West limb of Pico del Aguila tilting rate through

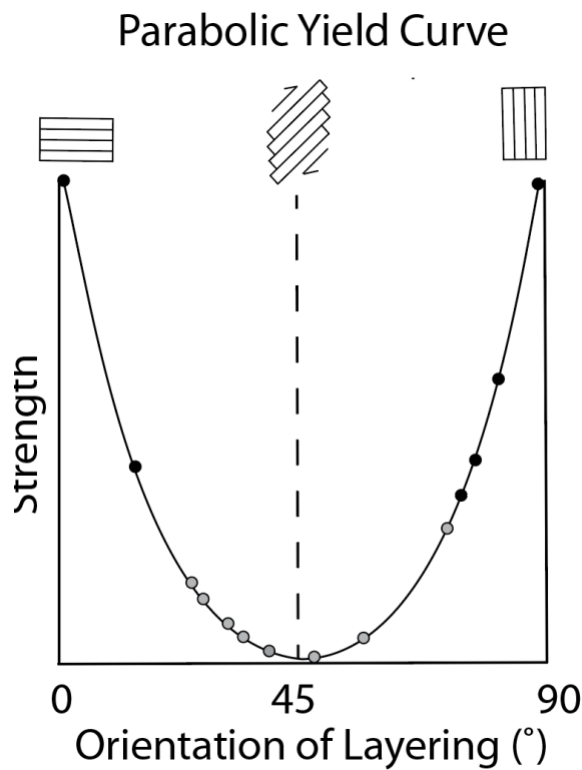
242 time. A. Each increment of folding is indicated by a box size equivalent to uncertainties in

243 folding rate and age. The errors in absolute age of the beginning and ending increments of

244 folding are assigned to be 10,000 years, according to the astrochronology constrained

245 increments, but ages are based on magnetic reversal chronology only. The second y-axis shows

246 the percent of tilting. The grey and black dot colors are maintained in **Figure 6** with times
 247 indicated by the grey dots representing extrinsic modulation of folding amounts and black dots
 248 indicating times of intrinsic modulation' **Figure 5B** shows the sediment accumulation rate
 249 determined from the tuned ARM time series of Kodama and Hinnov (2014). The duration of
 250 folding is indicated by the double-headed arrow. Correlation of accumulation rates and
 251 folding amounts documents the extrinsic modulation of folding rates. **1.** Time of initial intrinsic
 252 modulation, including a time of condensed sediment accumulation and no folding. **2.** Time period
 253 of rapid folding and extrinsic folding modulation **3.** Intrinsic modulation because of bedding
 254 orientation corresponding to the period of fold burial.



255
 256 **Figure 6.** Parabolic yield curve showing the same amounts of folding as in **Figure 5**. The strength
 257 is relative, and the figure shows the early and late periods of intrinsically modulated folding
 258 when layer orientation is expected to result in higher strength and the period of extrinsically
 259 modulated folding as a result of sedimentation variations.

260 Studies of stress during orogenesis reconstruct values that vary with measurement
261 technique and position within the orogen (e.g., Newman, 1994; Holl and Anastasio, 1995). Holl
262 and Anastasio (1993) report westward progradation of fluvial environments within the
263 transported wedge-top basin delta at 500 m/myr between 51 Ma and 43 Ma at Mediaño
264 anticline, nearly 50 km to the northeast of Pico del Aguila and Holl and Anastasio (1995) report
265 a reorientation of the principal shortening directions to E-W in the vicinity of the Boltaña lateral
266 ramp ~30 km northeast of Pico del Aguila.

267 Based on folding theory, the explosive amplification of the folding rate is predictable
268 (e.g., Hudelston, 1973). More surprising is the cessation of folding for >0.5 myr, well after
269 folding began and before further folding again commenced at increased rates before slowing to
270 conclusion (**Fig. 5**). A pause in deformation was also observed by Carrigan et al. (2018) for a
271 fault-propagation fold further east in the Pyrenees that the authors attributed to a pause in
272 thrusting in the studied fault-related fold. The cessation of folding correlates in time with a
273 period of slow synorogenic sedimentation, resulting in a condensed growth section as a result
274 of little sediment loading. At the base of the Arguis Fm. neritic facies with abundant glauconitic
275 strata attests to frequent diastems and slow sedimentation.

276 Shear strain between mechanical layers, however, is the critical variable for flexural
277 folding in layered rocks (e.g. Ramsey, 1967). An upward convex parabolic yield curve predicts
278 the folding rate curve for flexural folds with shear on bedding planes (the main surface of weak
279 anisotropy; **Fig. 6**). The attitude of horizontal bedding makes it more difficult to initiate folding.
280 Then as bedding rotates, it geometrically strain softens, minimizing the incremental stress and
281 strain required for further tilting as bedding rotates to moderate angles. As bedding continues

282 to steepen further folding becomes harder again (e.g., Donath, 1962; Fisher, 1990), and at tight
283 interlimb angles, folds lock-up due to geometric strain hardening. For example, at the Pico del
284 Aguila anticline, the folding rate diminished greatly in the Late Eocene when the interlimb angle
285 reached 55° and stopped altogether by the Early Oligocene, even though shortening in the
286 External Sierras continued until the Early Miocene (Anastasio, 1992).

287 **3.1 What Controlled The Rate Of Folding At Pico Del Aguila Anticline?**

288 Folding in the External Sierra gets progressively younger and the folding is of smaller
289 amplitude further west in the range, consistent with folding caused by differential loading
290 halotectonics (e.g. Anastasio, 1992; **Fig. 2**). Folding ceased when synorogenic sedimentation
291 was very slow and increased in a pulsating fashion as deltaic sedimentation rates varied (**Fig. 5**).
292 Coarsely gridded climate models by Sloan and Huber (2001) showed up to 15% variability in
293 river runoff at precessional frequencies in the strike parallel river feeding the wedge-top delta.
294 For the 2 myr, between 39.5 Ma and 37.5 Ma, the sediment accumulation rates around Pico del
295 Aguila varied with orbital forcing (**Fig. 5**). This is also the time period when limb tilting is
296 variable, beating in time with sedimentation rate. This time corresponds with modest bedding
297 inclination and cyclic sedimentary accumulation rates supporting the differential loading
298 hypothesis and the conclusion of extrinsic modulation of folding. Exposures of the incompetent
299 Triassic Pont de Suert Fm. (includes the Keuper facies evaporites and shales) in the Pico del
300 Aguila anticlinal core are everywhere deformed and the formation varies in thickness from 0 m
301 in synclinal salt welds to >2 km beneath the anticlines where the flowage of the Keuper facies
302 was greatest. What remains unclear is to what degree the incompetent Triassic Keuper facies
303 that cores the fold played in the transition from external to internal modulation. In models of

304 halotectonic folding driven by progradation, growing anticlines only continue to amplify while
305 the adjacent salt is deflating below the prograding sediment wedge (Ge et al., 1997). Once the
306 entirety of the mobile unit has been removed from the prograding wedge, the adjacent fold no
307 longer grows by amplification, but would simply migrate in front of the prograding sediments.
308 This conceptual model is consistent with the 3D restoration of Pico del Aguila by Vidal-Royo et
309 al., (2012), which indicated a late-stage switch from fold amplification to fold migration as
310 evidenced by the migration of the synclinal hinges.

311 Thrust faulting in the core of the Pico del Aguila décollement anticline breached the
312 lower Guara Fm. after fold tightening (e.g., Gonzalez-Mieres and Suppe, 2006; **Fig. 7**).



313
314 **Figure 7.** Field photograph of the core of Pico del Aguila, looking north. Late thrust fault
315 decapitating anticline in fold's core to accommodate fold tightening. Photograph view shown in
316 **Figure 1C.**

317
318 The pause in folding after initiation is recorded by constant dip and parallel beds in the growth
319 strata (**Fig. 4**). Climate cycles were expected to have caused both runoff variation in the
320 southern Pyrenees Paleogene rivers (e.g. Sloan and Huber, 2001) and variation in sedimentary
321 facies and progradation rates during the pause in folding at Pico del Aguila. The buried
322 geometry of Pico del Aguila is ridge-like to the north beneath the Jaca Basin. It is unlikely, that
323 river avulsion within the Paleogene delta and the resulting change in the locus of deposition

324 could have affected the variations in folding rate and river avulsion in deltaic environments is
325 likely to occur at a much faster rate than precessional frequencies, ranging from decades to
326 millennia (e.g. Hajek and Wolinsky 2012; Foreman and Straub, 2017), therefore, this processes
327 too, is unlikely to explain the folding rate behavior.

328 Initially (at 41.2 Ma - 38.9 Ma), folding rates were intrinsically controlled by shallow
329 bedding orientation. Following this initial stage, variations in boundary conditions began to
330 occur along the synorogenic surface. Here, climate affected runoff variation in the wedge-top
331 basin strike-parallel river, which in turn, controlled the deltaic sedimentation accumulation
332 rates around Pico del Aguila, the ultimate cause of the differential loading halotectonics. After
333 37.6 Ma, fold tightening led to geometric strain hardening and a slowing of folding rates (**Fig. 5**).
334 This was again, a time period of intrinsic fold modulation. The strain hardening then led to late-
335 stage contractional faulting in the fold's core. Gunderson et al. (2018) found similar evidence of
336 intrinsic modulation of deformation at 10^4 to 10^5 yr timescales in a study of thrusting rates
337 done in the central Apennines, Italy.

338 **4 CONCLUSIONS**

339 Using a high-resolution chronology of the growth strata surrounding Pico del Aguila
340 anticline, incremental folding rates were reconstructed for the buried fold. Folding at Pico del
341 Aguila occurred over an ~ 5.24 myr period at unsteady rates at 10^4 and 10^5 yr timescales. Monte
342 Carlo analysis of folding rate uncertainties, including spatial positions, bedding orientations,
343 growth strata geometries, chron boundary ages, and paleomagnetic site spacing, demonstrate
344 statistically significant variations in folding rates at the anticline. Folding rates varied between
345 $0^\circ \pm 5.5^\circ/\text{myr}$ and $90^\circ \pm 19^\circ/\text{myr}$. Folding temporarily ceased in the Late Eocene, then accelerated

346 to a maximum rate, and then decelerated once again toward the end of folding. Initially, folding
347 rates were controlled by intrinsic factors related to the shallow dip of bedding. Subsequent
348 variable folding rates are attributed to episodic sediment accumulation in the axial wedge-top
349 basin, an extrinsic modulation. Sediment accumulation rates increased as the delta prograded,
350 then folding rates began to respond to intrinsic modulation related to the steepening of Guara
351 Fm. bedding, with slower folding rates and late-stage thrust faulting occurring within the fold's
352 core.

353 **ACKNOWLEDGMENTS**

354 Field and laboratory research were assisted by Michael Newton and Christine Regalla,
355 Lehigh University and Jim Greenberg, UNAVCO, Inc. Research funding was provided by NSF EAR-
356 0409077. No authors have any real or perceived financial or affiliation conflicts of interest. Data
357 supporting the chronologic model of the growth strata were first published in Kodama et al.,
358 2010. This paper was written while the first author was a Visiting Professor at Centro Nacional
359 de Investigación sobre La Evolución Humana (CENIEH), Burgos, Spain. Kellen Gunderson is
360 thanked for his review of this manuscript. Juliet Crider and David Oakley are thanked for their
361 reviews of a previous version of the manuscript.

362 **REFERENCES CITED**

363 Anastasio, D. J. (1987) *Thrusting, Halotectonics, and Sedimentation in the External Sierra,*
364 *Southern Pyrenees, Spain* (Doctoral dissertation), Baltimore, Johns Hopkins University.
365 Anastasio, D. J. (1992) Structural Evolution of the External Sierra, Spanish Pyrenees. In S. Mitra,
366 S. and Fisher, G.W. eds., *The Structural Geology of Fold and Thrust Belts*, pp. 239-251,
367 Baltimore, MD, Johns Hopkins University Press.

368 Anastasio, D. & Holl, J. (2001) Transverse fold evolution in the External Sierra, southern
369 Pyrenees, Spain, *Journal of Structural Geology*, 23, 379-392.

370 Anastasio, D. J., Parés, J.M., Kodama, K.P., & Troy, J., Pueyo, E.M. (2015) Synsedimentary
371 Deformation at Pico del Aguila, Spain, recovered from AMS Data. In Pueyo, E.L., Cifelli, F.,
372 Sussman, A.J., Oliva-Urcia, B., (Eds.), *Palaeomagnetism in Fold and Thrust Belts: New*
373 *Perspectives*. Geological Society of London, Special Volume 425.
374 <https://doi.org/10.1144/SP425.8>

375 Bennett, R. A., Friedrich, A. M., & Furlong, K. P. (2004) Codependent histories of the San
376 Andreas and San Jacinto fault zones from inversion of fault displacement rates, *Geology*, 32
377 (11), 961-964.

378 Bishop, R. S. (1978) Mechanism of emplacement of piercement diapirs, *American Association of*
379 *Petroleum Geologists Bulletin*, 62, 1561-1583.

380 Burbank, D. W., Blythe, A. E., Putkonen, J., Pratt-Sitaula, B., Gabet, E., Oskin, M., Barros, A., &
381 Ojha, T. P. (2003) Decoupling of erosion and precipitation in the Himalayas, *Nature*, 426,
382 652-655.

383 Canudo, J. I. (1990) *Los foraminiferos planctonicos del Paleoceno-Eocene del Prepirineo oscense*
384 *en el sector de Arguis* (Doctoral dissertation), Zaragoza, Spain, University of Zaragoza.

385 Canudo, J. I., J. Malagon, A. Melendez, H. Millan, E. Molina, & Navarro, J. J. (1991) Las
386 secuencias deposicionales del Eoceno medio y superior de las Sierras exteriores (Prepirineo
387 meridional aragones), *Geogaceta*, 9, 81-84.

388 Carrigan, J. H., Anastasio, D. J., Kodama, K. P., & Parés, J. M. (2016) Fault-related fold kinematics
389 recorded by terrestrial growth strata, Sant Llorenç de Morunys, Pyrenees Mountains, NE

390 Spain, *Journal of Structural Geology*, 91, 161-176.

391 <http://dx.doi.org/10.1016/j.jsg.2016.09.003>

392 Castelltort, S., Guillocheau, F., Robin, C., Rouby, D., Nalpas, T., Lafont, F., & Eschard, R. (2003)

393 Fold control on the stratigraphic record: a quantified sequence stratigraphic study of the

394 Pico del Aguila anticline in the south-western Pyrenees (Spain), *Basin Research*, 15, 527-551.

395 Dolan, J. F., McAuliffe, L. J., Rhodes, E. J., McGill, S. F., & Zinke, R. (2016) Extreme multi-

396 millennial slip rate variations on the Garlock fault, California: Strain super-cycles, potentially

397 time-variable fault strength, and implications for system-level earthquake occurrence, *Earth*

398 *and Planetary Science Letters*, 446, 123–136. <https://doi.org/10.1016/j.epsl.2016.04.011>

399 Donath, F.A. (1962) Role of layering in geologic deformation. *Transactions New York Academy*

400 *of Sciences*, Series 2, 24, p. 236-249.

401 Donath, F. A. & Parker, R. B. (1964) Folds and folding, *Geological Society of America Bulletin*, 75,

402 45-62.

403 Fisher, D. M. (1990) Orientation history and rheology in slates, Kodiak and Afognak Islands,

404 Alaska, *Journal of Structural Geology*, 12, 483-498, [https://doi.org/10.1016/0191-](https://doi.org/10.1016/0191-8141(90)90036-X)

405 [8141\(90\)90036-X](https://doi.org/10.1016/0191-8141(90)90036-X)

406 Foreman, B. Z. & Straub, K. M. (2017) Autogenic geomorphic processes determine the

407 resolution and fidelity of terrestrial paleoclimate records. *Science Advances*, 3, e1700683.

408 Ge, H., Jackson, M. P. A., & Vendeville, B. C. (1997) Kinematics and dynamics of salt tectonics

409 driven by progradation, *American Association of Petroleum Geologists Bulletin*, 81, 398-423.

410 Gold, R. D., Cowgill, E., Arrowsmith, J. R., & Friedrich, A. M. (2017) Pulsed strain release on the
411 Altyn Tagh fault, northwest China, *Earth and Planetary Science Letters*, 459, 291-300,
412 <https://doi.org/10.1016/j.epsl.2016.11.024>

413 Gonzalez-Mieres, R. & Suppe, J. (2006) Relief and shortening in detachment folds, *Journal of*
414 *Structural Geology*, 28, 1785-1807.

415 Gradstein, F. M., Ogg, J. G. Schmitz, M. D., & Ogg, G. M. (2012) The Geologic Time Scale 2012,
416 First Edition. Elsevier B. V. <https://doi.org/10.1016/C2011-1-08249-8>

417 Gunderson, K. L., Anastasio, D. J., Pazzaglia, F. J., & Picotti, V. (2013) Fault slip rate variability on
418 10^4 - 10^5 yr timescales for the Salsomaggiore blind thrust fault, Northern Apennines, Italy,
419 *Tectonophysics*, 240, 356-365. <https://dx.doi.org/10.1016/j.tecto.2013.09.01>.

420 Gunderson, K. L., Pazzaglia, F. J., Picotti, V., Anastasio, D. A., Kodama, K. P., & Rittenour, T.,
421 2014. Unraveling tectonic and climatic controls on synorogenic growth strata (Northern
422 Apennines, Italy), *Geological Society of America Bulletin*, 126 (3-4), 532–552.
423 <https://doi.org/10.1130/B30902.1>

424 Gunderson, K. L., Anastasio, D. J., Pazzaglia, F. J., & Kodama, K. P. (2018) Intrinsically variable
425 blind thrust faulting, *Tectonics*, 37, 1454-1471.

426 Hajek, E. A. & Wolinsky, M. A. (2012) Simplified process modeling of river avulsion and alluvial
427 architecture: Connecting models and field data, *Sedimentary Geology*, 257, 1–30.

428 Hetzel, R. & Hampel, A. (2005) Slip rate variations on normal faults during glacial-interglacial
429 changes in surface loads, *Nature*, 435, 81-4. <https://doi.org/10.1038/nature03562>.

430 Hilgen, F., Kuiper, K., Krijgsman, W., Snel, E., & van der Laan, E. (2007) Astronomical tuning as
431 the basis for high resolution chronostratigraphy: the intricate history of the Messinian
432 Salinity Crisis, *Stratigraphy*, 4, 231-238.

433 Hogan, P.J. (1991) *Geochronologic, tectonic, and stratigraphic evolution of the Southwest*
434 *Pyrenean Foreland, Northern Spain* (Doctoral dissertation), Los Angeles, CA, University of
435 Southern California.

436 Hogan, P. J. & Burbank, D. W. (1996) Evolution of the Jaca piggyback basin and emergence of
437 the External Sierra, southern Pyrenees: In Friend, P.F., Dabrio, Cristino J., (Eds.), *Tertiary*
438 *Basins of Spain: The stratigraphic Record of Crustal Kinematics*. p. 153-160, Cambridge
439 England, Cambridge University Press.

440 Holl, J. E. & Anastasio, D. J. (1993) Paleomagnetically Derived Folding Rates, Southern Pyrenees,
441 Spain, *Geology*, 13 (3), 271-274.

442 Holl, J. E. & Anastasio, D. J. (1995) Kinematics around a large-scale oblique ramp, southern
443 Pyrenees, Spain, *Tectonics*, 14, 1368-1379.

444 Hudleston, P. J. 1973. Fold morphology and some geometrical implications of theories of fold
445 development, *Tectonophysics*, 16, 1-46.

446 Kodama, K. P., Anastasio, D. J., Newton, M. L., Pares, J. M., & Hinnov, L. A. (2010) High-
447 resolution rock magnetic cyclostratigraphy in an Eocene flysch, Spanish Pyrenees,
448 *Geochemistry. Geophysics, Geosystems*, 11, 1-22, QOAA07,
449 <https://doi.org/10.1029/2010GC003069>

450 Kodama, K. P. & Hinnov, L. A. (2014) *Rock Magnetic Cyclostratigraphy*. New York, NY, Wiley-
451 Blackwell. <https://doi.org/10.1002/9781118561294>

452 Laskar, J., Joutel, F. & Boudin, F. (1993) Orbital, precessional, and insolation quantities for the
453 earth from -20 Myr to +10 Myr. *Astronomy and Astrophysics*, 270,522-533.

454 Laskar, J. P., Robutel, F. Joutel, M. Gastineau, A. C. M. Correia, & Levrard, B. (2004) A long term
455 numerical solution for the insolation quantities of the Earth, *Astronomy and Astrophysics*,
456 428, 261–285. <https://doi.org/10.1051/0004-6361:20041335>

457 Lourens, L., Hilgen, F., Laskar, J., Shackleton, N. J., & Wilson D. (2004) The Neogene Period. A
458 Geologic Time Scale 2004. <https://doi.org/10.1017/CBO9780511536045.022>

459 McCartney, T. & Scholz, C. A. (2016) A 1.3 million year record of synchronous faulting in the
460 hangingwall and border fault of a half-graben in the Malawi (Nyasa) Rift, *Journal of*
461 *Structural Geology*, 91, 114-129.

462 Mey, P. H. W., Nagtegaal, P. J. C., Robert, K. J., & Hartvelt, J. A. A. (1968) Lithostratigraphic
463 subdivision of post-Hercynian deposits in the south central Pyrenees, Spain, *Leidsche*
464 *Geologische Mededelingen*, 41, 221-228.

465 Newman, J. (1994) The influence of grain size and grain size distribution methods for estimating
466 paleostresses from twinning in carbonates. *Journal of Structural Geology*, 16, 1598-1601.

467 Poblet, J. & Hardy, S. (1995) Reverse Modeling of Detachment Folds – Application to the Pico-
468 del-Aguila Anticline in the South Central Pyrenees (Spain), *Journal of Structural Geology*, 17,
469 1707-1710.

470 Puigdefàbregas, C. (1975) *La Sedimentation Molasica en la Cuenca de Jaca*. Monograph 104,
471 Jaca, Instituto de Estudios Pirenaicos.

472 Pueyo, E. L., Millán, H., & Pocoví, A. (2002) Rotation velocity of a thrust: a paleomagnetic
473 study in the External Sierras (Southern Pyrenees), *Sedimentary Geology*, 146, 191-

474 208.

475 Ramsey, J.G. (1967) *Folding and Fracturing of Rocks*. New York, NY, McGraw-Hill Book
476 Company.

477 Rodriguez-Pintó, A., Pueyo, E. L., Sierra-Kiel, J., Sanso, J. M., Barnolas, A., & Pocoví, A. (2012)
478 Lutition magnetostratigraphic calibration of larger foraminifera zonation (SBZ) in the southern
479 Pyrenees: The Isuela section, *Paleoecology, Paleoclimatology, Paleogeography*, 333, 107-120.

480 Sherwin, J. A. & Chapple, W. M. (1968) Wavelengths of single layer folds: a comparison
481 between theory and observation, *American Journal of Science*, 266, 167-179.

482 Sloan, L. C. & Huber, M. (2001) Eocene oceanic responses to orbital forcing on precessional
483 time scales, *Paleoceanography*, 16, 101–111, <https://doi.org/10.1029/1999PA000491>

484 Shaffer, D. M., Tobin, H. J. (2011) Hydrogeology and mechanics of subduction zone forearcs:
485 Fluid flow and pore pressure, *Annual Review of Earth and Planetary Sciences*, 39, 157-186.

486 Suppe, J., Chou, G. T., & Hook, S. K. (1992) Rates of folding and faulting determined from
487 growth strata. In, McClay, K.R. editor, *Thrust Tectonics*. p. 105-122, New York, NY, Springer,
488 ISBN 978-94-011-3066-0

489 Vidal-Royo, O., Cardozo, N., Muñoz, J. A., Hardy, S., & Maerten, L. (2012) Multiple mechanisms
490 driving detachment folding as deduced from 3D reconstruction and geomechanical
491 restoration: the Pico del Aguila anticline (External Sierras, Southern Pyrenees), *Basin
492 Research*, 24, 295-313, <https://doi.org/10.1111/j.1365-2117.2011.00525>

493 Vidal-Royo, O., Muñoz, J. A., Hardy, S., Koyi, H., & Cardozo, N. (2013) Structural evolution of
494 Pico de Aguila anticline (External Sierras, southern Pyrenees) derived from sandbox,
495 numerical and 3D structural modeling techniques, *Geologica Acta*, 11, 1-26.